TRANSITION OF SUPERSONIC PLANE JET DUE TO SYMMETRIC/ANTISYMMETRIC UNSTABLE MODES

Daisuke Watanabe
Department of Mechanical and Control Engineering,
the University of Electro-Communications
182-8585 Tokyo, Japan
watanabe@maekawa.mce.uec.ac.jp

Hiroshi Maekawa
Department of Mechanical Engineering and Intelligent Systems,
the University of Electro-Communications
182-8585 Tokyo, Japan
maekawa@mce.uec.ac.jp

ABSTRACT

Results from linear stability analysis are presented for widely variety of top-hat plane jets, including viscous effects and high convective Mach number plane jets. It is found that the dominant mode is 2-D antisymmetric mode for Mc less than 0.8, 3-D antisymmetric mode for Mc larger than 0.8 and less than 1.5, and 2-D symmetric mode (S2) for Mc larger than 1.5. Direct numerical simulations of spatially developing 2-D and temporally developing 3-D are performed using high-order compact schemes. 2-D DNS and stability analysis show that S2 instability mode nature prohibits vortex pairing in the flow field for high Mc numbers. 3-D simulations for Mc=1.13 show sound field are observed when (0,2) modes become dominant after saturation of oblique modes.

INTRODUCTION

A fundamental problem in the study of compressible shear flows is the analysis of compressible jets, which can be found in such diverse contexts as rocket, scramjet, ramjet, turbofan and turbojet engines. Recently and with the new noise regulations, reducing jet engines acoustic emissions became a major challenge for aircraft designers and manufacturers (see Lele[1],Colonius[2],Mitchell[3] et al.). The understanding of the effect of jet structures on the noise generation (acoustic waves) is very crucial for noise control. Therefore and in this challenging context, we investigated the linear stability of high Mach number plane jets, then, and by means of DNS, the development of the corresponding supersonic flow structures after being perturbed with the unstable modes.

COMPUTATIONAL DETAILS

In this work, the linearized, three-dimensional, viscous, compressible, parallel flow disturbance equation representing the equations of state, mass conservation, x_1- x_2-, x_3-momentum, and energy are considered. All nondmensionalized flow variables are decomposed into a mean and fluctuating component as $d = \bar{d} + \tilde{d}$.

We employed the mean velocity profile given by

$$\bar{u}_1(x_2) = \frac{U}{2}\left[1 - tanh\left[\frac{12.5}{4}\left(\frac{x_2}{b} - \frac{b}{x_2}\right)\right]\right]. \quad (1)$$

The disturbances were assumed in the form of normal modes.

$$\widetilde{d}(\widetilde{\rho}, \widetilde{u}_1, \widetilde{u}_2, \widetilde{u}_3, \widetilde{T}) = \hat{d}_{3D}(\hat{\rho}, \hat{u}_1, \hat{u}_2, \hat{u}_3, \hat{T}) \times exp[i(\alpha x_1 + \beta x_3 - \omega t)] \quad (2)$$

The angle of the disturbance with respect to the streamwise direction is given by

$$\theta = \tan^{-1}(\beta/\alpha). \quad (3)$$

The linearizing disturbance equations solved using a mapped spectral method,

$$x_2 = h(\zeta) = -acot(\pi\zeta)(0 \le \zeta \le 1), (-\infty \le \zeta \le \infty), \quad (4)$$

and are formulated as a 5×5 matrix eigenvalue problem

$$\mathbf{A}\hat{d}_{3D} = \omega \hat{d}_{3D} \quad (5)$$

where

$$\mathbf{A} = \begin{pmatrix} \alpha\overline{u}_1 & \alpha\overline{\rho} & -i(D\overline{\rho} + \overline{\rho}D) & \beta\overline{\rho} & 0 \\ \frac{\alpha\overline{T}}{\overline{\rho}\gamma M^2} & a_{22} & a_{23} & -\frac{i\overline{\mu}\alpha\beta}{3\overline{\rho}Re} & a_{25} \\ -\frac{i(D\overline{T}+\overline{T}D)}{\overline{\rho}\gamma M^2} & a_{32} & a_{33} & a_{34} & a_{35} \\ \frac{\beta\overline{T}}{\overline{\rho}\gamma M^2} & -\frac{i\alpha\beta\overline{\mu}}{3\overline{\rho}Re} & a_{43} & a_{44} & \frac{\beta}{\gamma M^2} \\ 0 & a_{52} & a_{53} & (\gamma-1)\beta\overline{T} & a_{55} \end{pmatrix} \quad (6)$$

$$D \equiv d/dx_2, D^2 \equiv d^2/dx_2^2$$

$$a_{22} = \alpha\overline{u}_1 - \frac{i}{\overline{\rho}Re}\left\{\overline{\mu}\left(\frac{4}{3}\alpha^2 - D^2 + \beta^2\right) - \frac{d\overline{\mu}}{d\overline{T}}D\overline{T}D\right\}$$
$$a_{23} = -iD\overline{u}_1 - \frac{\alpha}{\overline{\rho}Re}\left(\frac{1}{3}\overline{\mu}D + \frac{d\overline{\mu}}{d\overline{T}}D\overline{T}\right)$$
$$a_{25} = \frac{\alpha}{\gamma M^2}$$
$$+\frac{i}{\overline{\rho}Re}\left(D\overline{u}_1\frac{d^2\overline{\mu}}{d\overline{T}^2}D\overline{T} + \frac{d\overline{\mu}}{d\overline{T}}D^2\overline{u}_1 + D\overline{u}_1\frac{d\overline{\mu}}{d\overline{T}}D - D\overline{u}_1\frac{d\overline{\mu}}{d\overline{T}}D\overline{T}\right)$$
$$a_{32} = -\frac{\alpha}{\overline{\rho}Re}\left(\frac{1}{3}\overline{\mu}D - \frac{2}{3}\frac{d\overline{\mu}}{d\overline{T}}D\overline{T}\right)$$
$$a_{33} = \alpha\overline{u}_1 - \frac{i}{\overline{\rho}Re}\left\{\overline{\mu}\left(\alpha^2 - \frac{4}{3}D^2 + \beta^2\right) - \frac{4}{3}\frac{d\overline{\mu}}{d\overline{T}}D\overline{T}D\right\}$$
$$a_{34} = -\frac{\beta}{\overline{\rho}Re}\left(\frac{1}{3}\overline{\mu}D - \frac{2}{3}\frac{d\overline{\mu}}{d\overline{T}}D\overline{T}\right)$$
$$a_{35} = -\frac{i(D\overline{\rho}+\overline{\rho}D)}{\overline{\rho}\gamma M^2} - \frac{\alpha}{\overline{\rho}Re}D\overline{u}_1\frac{d\overline{\mu}}{d\overline{T}}$$
$$a_{43} = -\frac{\beta}{\overline{\rho}Re}\left(\frac{1}{3}\overline{\mu}D + \frac{d\overline{\mu}}{d\overline{T}}D\overline{T}\right)$$
$$a_{44} = \alpha\overline{u}_1 - \frac{i}{\overline{\rho}Re}\left\{\overline{\mu}\left(\alpha^2 - D^2 + \frac{4}{3}\beta^2\right) - \frac{d\overline{\mu}}{d\overline{T}}D\overline{T}D\right\}$$
$$a_{52} = \alpha(\gamma-1)\overline{T} + \frac{2i\gamma(\gamma-1)M^2\overline{\mu}}{\overline{\rho}Re}D\overline{u}_1 D$$
$$a_{53} = -i\{D\overline{T} + (\gamma-1)\overline{T}D\} - \frac{2\gamma(\gamma-1)M^2\overline{\mu}}{\overline{\rho}Re}\alpha D\overline{u}_1$$
$$a_{55} = \alpha\overline{u}_1 + \frac{i\gamma(\gamma-1)M^2}{\overline{\rho}Re}\frac{d\overline{\mu}}{d\overline{T}}(D\overline{u}_1)^2$$
$$-\frac{i\gamma}{\overline{\rho}RePr}\left\{\overline{\mu}(\alpha^2 - D^2 + \beta^2)\right.$$
$$\left. -\frac{d^2\overline{\mu}}{d\overline{T}^2}(D\overline{T})^2 - \frac{d\overline{\mu}}{d\overline{T}}\left(2D\overline{T}D + D^2\overline{T}\right)\right\}$$

for $i = j$

$$c_{ij} = -\frac{(N-1)}{aN}sin(2\pi\zeta), \tag{7}$$

for $i \neq j$

$$c_{ij} = -\frac{1}{2a}\{\cos(2\pi\zeta_j) - 1\}(-1)^{i-j}\cot\frac{\pi(i-j)}{N} - \frac{1}{Na}\{\sin(2\pi\zeta_j)\}\frac{\sin\{(1-1/N)\pi(i-j)\}}{\sin\{\pi(i-j)/N\}}, \tag{8}$$

for $i = j$

$$d_{ij} = -\frac{1}{2Na^2}\{\cos(4\pi\zeta_j) - 4\cos(2\pi\zeta_j) + 3\}\frac{1}{3}(\frac{N}{2} - 1)\frac{N}{2}(N-1) - \frac{N-1}{Na^2}\{\cos(4\pi\zeta_j) - \cos(2\pi\zeta_j)\}, \tag{9}$$

for $i \neq j$

$$d_{ij} = -\frac{(-1)^{i-j}}{4a^2}\{\cos(4\pi\zeta_j) - 4\cos(2\pi\zeta_j) + 3\}\left(\frac{1}{\sin^2\{\pi(i-j)/N\}} - \frac{N}{2}\right) - \frac{3(-1)^{i-j}}{4a^2}\{2\sin(2\pi\zeta_j) - sin(4\pi\zeta_j)\}\cot\frac{\pi(i-j)}{N} - \frac{1}{Na^2}\{\cos(4\pi\zeta_j) - \cos(2\pi\zeta_j)\}\frac{\sin\{(1-1/N)\pi(i-j)\}}{\sin\{\pi(i-j)/N\}}. \tag{10}$$

In the direct numerical simulations, the following nondimensional equations governing the conservation of mass, momentum, and energy for a compressible Newtonian fluid were solved using sixth-order compact finite difference schemes[4] in all directions. The governing equations nondimensionalized by the characteristic physical scales, such as the half-width of b, are given as follows:

$$\frac{\partial\rho}{\partial t} + \frac{\partial(\rho u_i)}{\partial x_i} = 0, \tag{11}$$

$$\frac{\partial(\rho u_i)}{\partial t} + \frac{\partial(\rho u_i u_j)}{\partial x_j} = -\frac{\partial p}{\partial x_i} + \frac{\partial\tau_{ij}}{\partial x_j}, \tag{12}$$

$$\frac{\partial E_T}{\partial t} + \frac{\partial(E_T u_j)}{\partial x_j} = -\frac{\partial(pu_j)}{\partial x_j} + \frac{\partial(u_i\tau_{ij})}{\partial x_j} - \frac{\partial q}{\partial x_j} \tag{13}$$

where

$$E_T = \frac{p}{(\gamma-1)} + \frac{\rho u_i u_i}{2}, \tag{14}$$

$$q = -\frac{\mu}{(\gamma-1)M^2RePr}\frac{\partial T}{\partial x_i}, \tag{15}$$

$$\tau_{ij} = \frac{\mu}{Re}\left[\left(\frac{\partial u_i}{\partial x_j} + \frac{\partial u_j}{\partial x_i}\right) - \frac{2}{3}\delta_{ij}\frac{\partial u_k}{\partial x_k}\right], \tag{16}$$

$$T = \frac{\gamma M^2 p}{\rho}, \tag{17}$$

$$\mu = T^{2/3}. \tag{18}$$

Time advancement was performed by fourth-order Runge-Kutta algorithm. For 2-D spatial case, the computational mesh was $N_{x_1} \times N_{x_2} = 600 \times 300$ and for 3-D temporal case, the computational mesh was $N_{x_1} \times N_{x_2} \times N_{x_3} = 200 \times 200 \times 100$.

RESULTS

Linear stability

2D. Figure 1 is the results of linear stability analysis when $\beta = 0$ ($\theta = tan^{-1}(\beta/\alpha)$) for Re=1000 and Mc less than 0.75. (Mc stands for convective Mach number) Horizontal and vertical axes are wave number α and linear growth rate ω_i respectively. The curve plotted the eigenvalue of largest growth rate for each α. Continuous line, dashed line, and dotted line represent results of Mc=0.38, Mc=0.57 and Mc=0.75 respectively. Bold line corresponds to antisymmetric mode (hereafter referred to as A1) and fine line corresponds to symmetric mode (hereafter referred to as S1). For convective Mach number less than 0.75, two unstable modes A1 and S1 exist, but in this range, the antisymmetric mode is dominant. With the increase of Mc, the growth rates of these modes decrease, however the growth rate of the S1 decreases quicker than A1. In Mc=0.85, there is no positive growth rate of S1 mode.

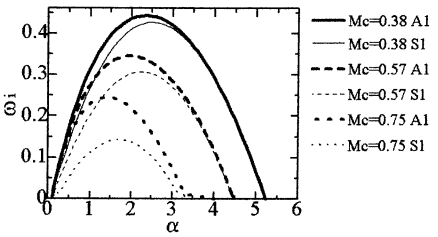

Figure 1: Effect of Mach number on the growth rate of 2-D waves for Mc=0.38-0.75 and Re=1000.

Figures 2 correspond to higher Mach number case. In this Mach number range, unstable modes, other than A1, show the largest growth rate at higher wave numbers. In Mc=1.51, five antisymmetric and symmetric modes appeared alternatively, therefore we called them A1, S2, A2, S3, A3 respectively. S2 mode which appears first by the increase in Mc is symmetrical, and this mode becomes dominant over Mc=1.13. Kudryavtsev[5] performed spatial 2-D DNS of Mc=1.5 plane jet that can be considered as a validation to our findings. From the analysis of the eigenfunction, it was proven that S2 mode differed from the S1 mode.

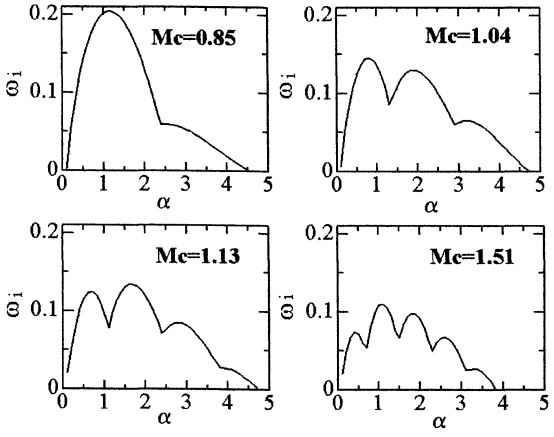

Figure 2: Effect of Mach number on the growth rate of 2-D waves for Mc=0.85-1.51 and Re=1000.

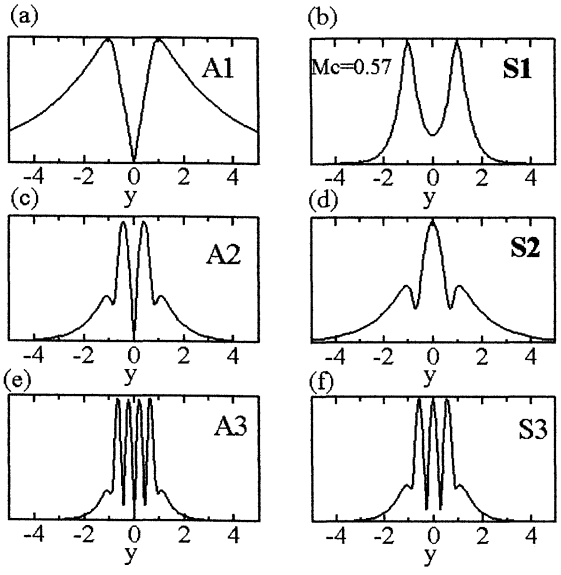

Figure 3: Eigenfunctions of pressure; (a)A1 mode, (b)S1 mode, (c)A2 mode, (d)S2 mode,(e)A3 mode, (f)S3 mode for Mc=1.51 and Re=1000.

Pressure eigenfunctions at Mc=1.51 (only S1 mode corresponds to Mc=0.57) are shown in Figures 3. In this figure, the maximum magnitudes of the S1 mode eigenfunction is located in both sides of jet center and S2 mode eigenfunction is located at jet center and the both sides, which implies that S2 is different from S1. Besides the number of eigenfunction's maximal magnitudes of A1 and S1 which have 2 peaks, S2, A2, S3 and A3 have 3, 4, 5 and 6 peaks respectively.

3D. Figures 4 is the result of linear stability analysis for Re=1000. Varying the Mach number affects the dominant mode. For Mc less than 0.8, the dominant mode is 2-D A1. For Mach number larger than 0.8 and less than 1.5 the most unstable mode is 3-D A1, and near Mc=1.13, the dominant 2-D mode changes from A1 to S2. For Mc over 1.5, the dominant mode is 2-D S2.

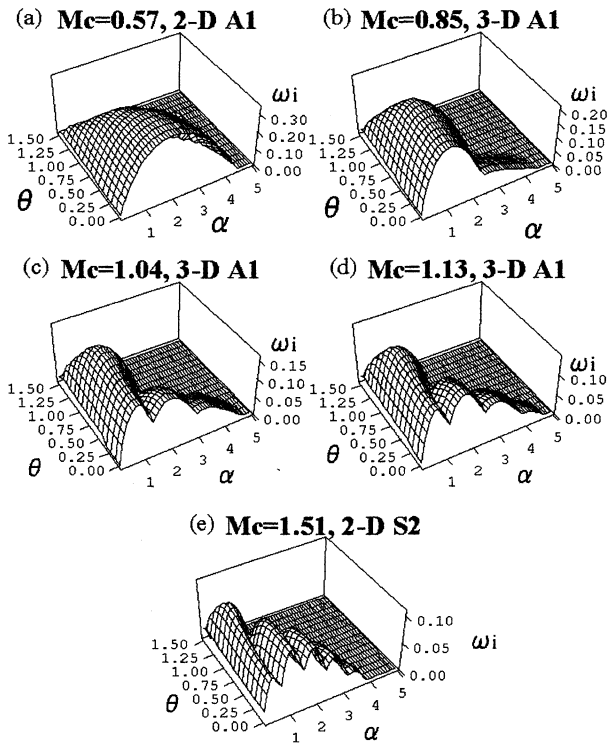

Figure 4: Effect of q on the growth rate of 3-D waves; (a)Mc=0.57, (b)Mc=0.85, (c)Mc=1.04, (d)Mc=1.13, (e)Mc=1.51 for Re=1000.

DNS

2D. Two-dimensional spatial direct numerical simulations were performed to investigate the vortical structures and sound fields after the development of A1, S1 and S2 modes for Re=1000. In these simulations we used antisymmetric and/or symmetric disturbances with broadband noise to perturb the normal velocity at the inlet. Simulations with three

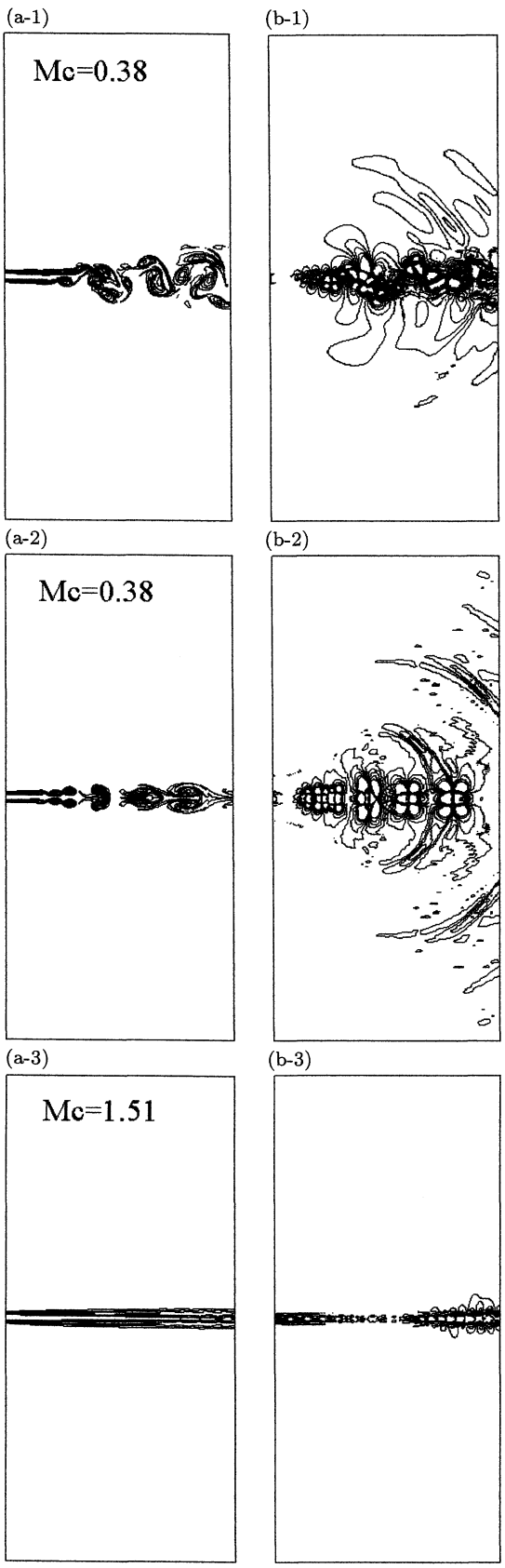

Figure 5: Contour plots of (a) vorticity and (b) dilatation; (a-1) (b-1) case 1 (A1) (Mc=0.38), (a-2) (b-2) case 1 (S1) (Mc=0.38), and (a-3) (b-3) case2 (S2) (Mc=1.51) for Re=1000.

initial conditions were carried out. In Case 1(A1), Mc=0.38 and we used antisymmetric and symmetric disturbances. In Case 1(S1), Mc=0.38 and we used only symmetric disturbances. In Case 2, Mc=1.51 and we used antisymmetric and symmetric disturbances. (Note that in Case 1(S1), only symmetrical disturbance was used because A1 mode grows faster than S1 mode.) The vorticity and sound fields are shown in Figures 5(a) and 5(b) respectively. The contour increments are the same. In Case 1(A1), the vortical field becomes asymmetric with regard to jet centerline, since the antisymmetric mode is dominant. In Case 1(S1), the vorticity field becomes symmetrical due to the growth of the S1 mode, because it was forced only with the symmetrical disturbance. In Case 2, the vorticity field becomes symmetric with regard to jet centerline, since the symmetric mode is dominant and its growth rate is larger than the antisymmetric one. In Case 1(A1) and Case 1(S1), there are pairings of the vortices, but in Case 2, there are no pairings in this computational region. From Figures 5(b), we can see the generation of acoustic waves in Case 1(A1) and Case 1(S1), however the dilatation field of the Case 1(S1) is stronger than the Case 1(A1). In Case 2, acoustic waves can't be seen clearly. The difference of these acoustic fields is explained by vortex pairing, present in Case 1 and absent in Case 2. This absence can be explained by the specified subharmonic modes.

In Figures 6, the comparison of the subharmonic modes growth rates shows that S1 is unstable at low wave numbers, however S2 is not unstable. From this fact, we conjecture that no pairing of the vortices in the flow fields is due to less development of S2 subharmonic mode. Therefore, the generation of the acoustic waves is very weak. Unfortunately, it could not be confirmed here, but we believe that the effect of A1 mode could appear in the far downstream.

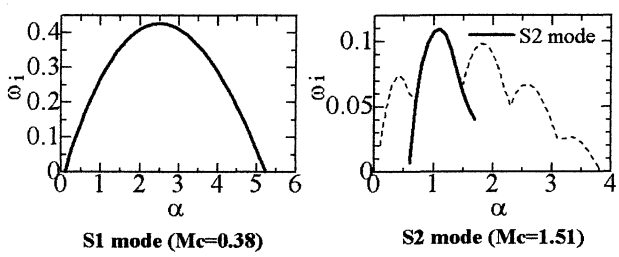

Figure 6: Comparison between subharmonic modes of S1 and S2.

3D. Three-dimensional temporal direct numerical simulations were performed to investigate flow structures and noise generation due to 2-D symmetric (2-D S2) and 3-D antisymmetric (3-D A1) modes. The mean profile was forced with the most unstable 2-D and a pair of oblique 3-D modes. The amplitude of the disturbances was about 1% of the jet velocity. The simulations with two initial conditions were carried out. In Case 1, the amplitudes of the 2-D and 3-D disturbances ($\theta = \pm 51$) were 1% and 0.5 % of the jet velocity. In Case 2, the amplitudes of the 2-D and 3-D disturbances ($\theta = \pm 51$) were 1% of the jet velocity.

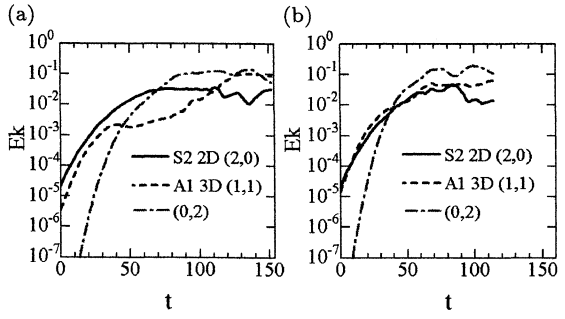

Figure 7: Time development of mode's kinetic energies for S2 2-D mode(2,0), A1 3-D mode (1,1) and (0,2); (a) Case 1, (b) Case 2 for Mc=1.13 and Re=1000.

Figures 7 shows the time development of mode's kinetic energies. In this Mach number, linear growth rate of 3-D A1 mode (1,1) is larger than 2-D S2 (2,0) one, however in Case 1 the energy growth of 3-D modes is suppressed by grown up 2-D mode. In Case 2, the energy of 3-D A1 mode became close to the 2-D S2 one, and 3-D A1 mode is suppressed weakly at around t=40 (In case 1,it was around t=36), while the 2-D S2 one has been amplified. Following the suppression of the 3-D A1 mode, in both cases, (0,2) Fourier component rapidly grows in comparison with other mode, later it becomes a dominant mode sooner in Case 2. The development of (0,2) mode leads to 3-D structures in the plane jet.

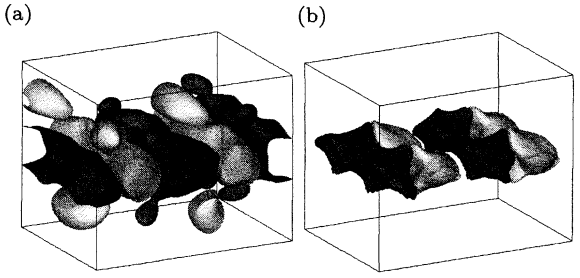

Figure 8: Iso-surfaces of (a) pressure; (b) dilatation at t=64 for Case1, Mc=1.13 and Re=1000.

Figures 8 shows the developed structures of 3-D flow motions from the prescribed initial condition for the Case 1 at t=64. This time, the energy of the S2 2-D mode saturates. Right and left figures show the pressure and dilatation fields respectively. In the right figure, the maximum value of the pressure exists around the jet center plane, as linear stability eigenfunction predicted it, but no significant three-dimensional structures were found. As for the acoustic filed, the very strong dilatation is formed around the jet center plane but the acoustic filed is weak in the far field.

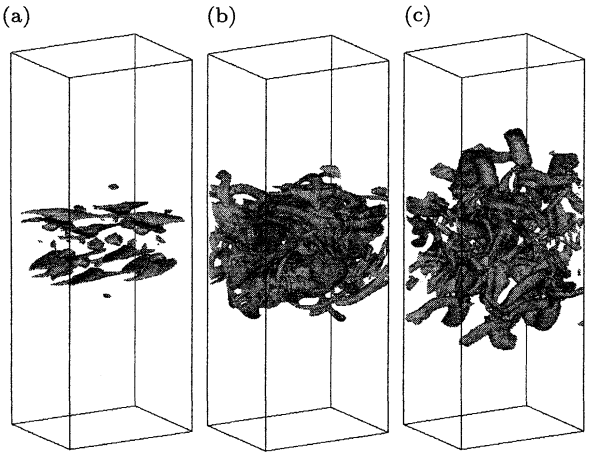

Figure 9: Iso-surface of second invariant of velocity gradient tensor, $Q = 0.1$, at (a) t=80, (b) t=120 and (c) t=152 for Case1, Mc=1.13 and Re=1000.

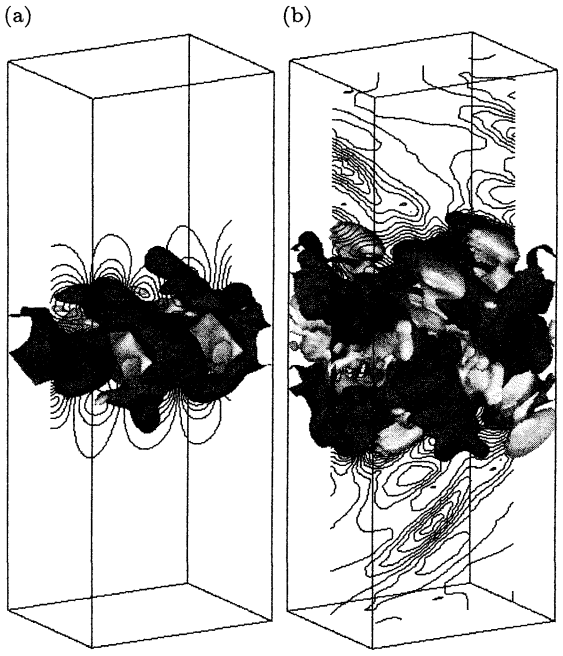

Figure 10: Iso-surfaces and contourplots of pressure at (a) t=80 and (b) t=120 for Case1, Mc=1.13 and Re=1000.

Figures 9 and 10 show the 3-D vortical structures and pressure fields for Case 1, respectively. Figure 9 presents a successive snap shots of the second invariant Q structures at t=80, 120 and 152. Note that a potential core

exists at t=80. At t=120, however, 3-D oblique modes are dominant, as shown in Figures 7, the potential core disappeared. The complicated structures of vortex tube are formed at t=120. At t=152, the tube-like structures spread outside. In Figure 10, due to the 3-D structure formation, the pressure fluctuations are observed outside at t=120, although no pressure fluctuation in the far field is observed at t=80.

Figures 11 and 12 show the dilatation fields and the v fluctuations averaged in the x-z plane for Case 1 and Case 2, respectively. Note that acoustic waves of div**u** propagate outside around t=80 for Case 1 and t=50 for Case 2. Figures 12 shows that the corresponding v fluctuations appear in the far field at that time. Around t=80 for Case 1 and t=50 for Case 2, the A1-3D and/or (0,2) modes become dominant and the sound field can be observed.

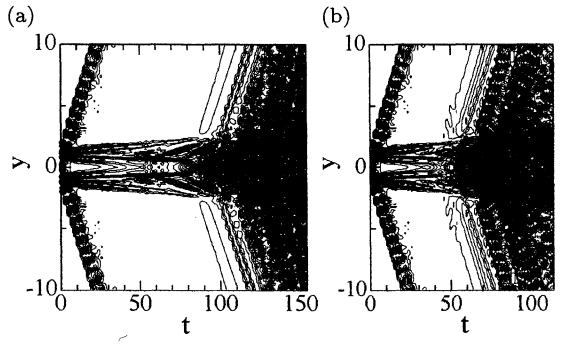

Figure 11: Time developments of mean dilatation ($\widehat{div}\mathbf{u}(y,0,0)$); (a) Case1 and (b) Case2 for Mc=1.13 and Re=1000.

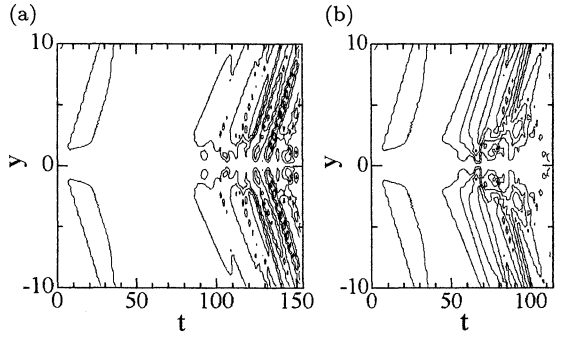

Figure 12: Time developments of mean normal velocity ($\hat{v}(y,0,0)$); (a) Case1 and (b) Case2 for Mc=1.13 and Re=1000.

SUMMARY

Linear stability analyses and direct numerical simulations of Supersonic Plane Jet were performed. From the linear stability study, we found that the dominant mode depends upon the Mach numbers. Two-dimensional spatial DNS show difficulty of pairing of the vortices in a flow where S2 is dominant. Therefore, the generation of the acoustic waves is very weak. In the three-dimensional temporal DNS, at Mc=1.13, it was confirmed that the structure of the flow field depended on the initial conditions, because the linear growth rates of the 2-D S2 and 3-D A1 modes were almost the same. When (0,2) mode becomes dominant, the dilatation sound fields were observed.

ACKNOWLEDGMENTS

This work was supported with a grant-in-aid (No.12004713) from the Japanese Ministry of Education and Culture. Some of the simulations were executed at the Information Technology Center of the University of Tokyo.

REFERENCES

Lele, S. K., and Moin, P., 1998, "Direct Simulation of a Mach 1.92 Jet and its sound field", *AIAA/CEAS.*, Vol. 98-2291, pp 1-12.

Colonius, T., Lele, S. K. and Moin, P., 1997, "Sound generation in a mixing layer" ,*J. Fluid Mech.*, Vol. 330, pp 375-409.

Mitchell, B. E., Lele, S. K. and Moin, P., 1999, "Direct computation of the sound generated by vortex pairing in an axisymmetric jet",*J. Fluid*, Vol. 383, pp 113-142.

Lele, S. K., 1992, "Compact Finite Difference Schemes with Spectral-like Resolution", *J. Comput. Phys.*, Vol. 103, pp. 16-42.

Kudryavtsev, A. and Khotyanovsky, D., 2000, "Numerical simulation of the spatial evolution of the instabilities in a supersonic plane jet",*Proceedings, 8th Advances in Turbulence*, pp. 161-164.